Electronic Supplementary Material (ESI) for Journal of Materials Chemistry C.

Supporting Information

Structural and Physical Properties of Two Distinct 2D Lead Halides with Intercalated Cu(II)

Kanika Parashar[a], Zheng Zhang[b], Volodymyr Buturlim[c], Jie Jiang[d], Alexander Roseborough[e], May Nyman[e] , Krzysztof Gofryk[c] , Ruth Pachter[d], Bayram Saparov[a*]

[a]Department of Chemistry & Biochemistry, The University of Oklahoma, Norman, Oklahoma 73019-5251, United States

[b]Department of Chemistry, Tulane University, New Orleans, Louisiana 70118, United States

[c]Glenn T. Seaborg Institute, Idaho National Laboratory, Idaho Falls, ID 83415, USA

[d]Materials and Manufacturing Directorate, Air Force Research Laboratory, Wright-Patterson Air Force Base, OH 45433, USA

[e]Department of Chemistry, Oregon State University, Corvallis, Oregon 97331, USA

*Author to whom correspondence should be addressed: saparov@ou.edu

Table S1. Selected single crystal data and structure refinement parameters for $[Cu(O_2C\text{-}CH_2\text{-}NH_2)_2]Pb_2Br_4$ and $[Cu(O_2C\text{-}(CH_2)_3\text{-}NH_3)_2]PbBr_4$.

Formula	**$[Cu(O_2C\text{-}CH_2\text{-}NH_2)_2]Pb_2Br_4$**	**$[Cu(O_2C\text{-}(CH_2)_3\text{-}NH_3)_2]PbBr_4$**
Formula weight (g/mol)	945.68	796.61
Temperature (K)	100(2)	100(2)
Wavelength (Å)	0.71073	0.71073
Crystal system	Monoclinic	Monoclinic
Space group	$P2_1/c$	$P2_1/n$
Z	2	4
Unit cell parameters (Å)	a = 8.5509(2) b = 10.9451(3) c = 8.3697(2) β = 108.700(10)°	a = 8.4521(7) b = 8.3195(7) c = 26.858(2) β = 98.396(3)°
Volume (Å^3)	741.97(3)	1868.4(3)
Density (g/cm^3)	4.233	2.832
Absorption coefficient (μ) (mm^{-1})	34.826	18.701
θ_{min} - θ_{max} (°)	3.129 to 26.370	2.444 to 33.787
Reflections collected	40882	77900
Independent reflections	1515	7485
R^a indices ($I > 2\sigma(I)$)	R_1 = 0.0131 wR_2 = 0.0298	R_1 = 0.02777 wR_2 = 0.0696
Goodness-of-fit on F^2	1.128	1.023
Largest diff. peak and hole (e$^-$/Å^3)	0.768 and -0.651	1.433 and -1.649

$$_aR_1 = \sum\big||F_0| - |F_c|\big| / \sum|F_0|;\ wR_2 = \ |\Sigma|w(F_0^2 - F_c^2)^2 / \sum\left|wF_0^{22}\right|_{1/2}$$

where $w = 1/\left|\sigma^2F_0^2 + (AP)^2 + BP\right|$, with $P = (F_0^2 + 2F_c^2)/3$ and weight coefficients A and B

Table S2. Atomic coordinates and equivalent isotropic displacement parameters (U_{eq}[a]) for $[Cu(O_2C\text{-}CH_2\text{-}NH_2)_2]Pb_2Br_4$.

Atom	***x***	***y***	***z***	U_{eq}, **Å²**
Pb1	0.5919(2)	0.70010(2)	0.63273(2)	0.01903(6)
Br1	0.60133(4)	0.44554(3)	0.72215(4)	0.01925(8)
Br2	0.79076(4)	0.75829(3)	0.97054(4)	0.02220(9)
Cu1	0.0000000	0.5000000	0.5000000	0.02486(14)
O1	0.3613(3)	0.6614(2)	0.8544(3)	0.0244(5)
O2	0.2003(3)	0.5971(2)	0.6073(3)	0.0207(5)
N1	0.0014(4)	0.4709(3)	0.7322(3)	0.0223(6)
C1	0.2335(4)	0.6095(3)	0.7650(4)	0.0174(6)
C2	0.1134(4)	0.5582(3)	0.8463(4)	0.0240(7)

[a] U_{eq} is defined as one third of the trace of the orthogonalized U_{ij} tensor.

Table S3. Atomic coordinates and equivalent isotropic displacement parameters (U_{eq}[a]) for $[Cu(O_2C\text{-}(CH_2)_3\text{-}NH_3)_2]PbBr_4$.

Atom	*x*	*y*	*z*	U_{eq}, Å^2
Pb1	0.50976(2)	0.49993(2)	0.24772(2)	0.01877(4)
Br1	0.54891(4)	0.39650(4)	0.35970(2)	0.02523(7)
Br2	0.23518(4)	0.72381(4)	0.26259(2)	0.02740(7)
Br3	0.42664(5)	0.54648(5)	0.14119(2)	0.03332(8)
Br4	0.70424(5)	0.79916(5)	0.26455(2)	0.03641(9)
Cu1	0.52222(4)	0.44714(4)	0.45518(2)	0.01714(7)
O1A	0.6224(3)	0.6581(3)	0.45384(9)	0.0270(5)
O2A	0.5813(3)	0.7530(3)	0.52866(9)	0.0308(5)
N1A	0.4825(5)	1.0084(4)	0.34069(14)	0.0362(8)
C1A	0.6289(4)	0.7669(3)	0.48674(11)	0.0203(5)
C2A	0.6968(4)	0.9276(4)	0.47421(12)	0.0237(6)
C3A	0.6785(4)	0.9630(4)	0.41764(13)	0.0269(6)
C4A	0.5053(4)	0.9549(5)	0.39442(13)	0.0302(7)
O1B	0.3076(3)	0.5444(3)	0.43678(9)	0.0292(5)
O2B	0.2727(3)	0.6374(3)	0.51208(8)	0.0278(5)
N1B	0.1316(4)	0.4457(4)	0.34737(11)	0.0307(6)
C1B	0.2244(4)	0.6107(4)	0.46665(12)	0.0212(5)
C2B	0.0558(4)	0.6594(4)	0.44612(13)	0.0287(7)
C3B	-0.0385(5)	0.5391(6)	0.41049(17)	0.0419(9)
C4B	-0.0132(6)	0.5377(7)	0.35657(17)	0.0479(11)

[a] U_{eq} is defined as one third of the trace of the orthogonalized U_{ij} tensor.

Table S4. A comparison of bond distances and angles within the $PbBr_5O_3$ dodecahedra in $[Cu(O_2C\text{-}CH_2\text{-}NH_2)_2]Pb_2Br_4$.

Atom pair	**Distance (Å)**	**Label**	**Angle (°)**
Pb1 – O1	2.593(2)	O1 – Pb1 – O1	120.20(9)
Pb1 – O1	2.727(2)	O1 – Pb1 – Br1	79.29(6)
Pb1 – Br1	2.9265(3)		
Pb1 – Br2	3.1355(3)	Br1 – Pb1 – Br2	78.33(5)
Pb1 – Br2	3.1532(3)	Br2 – Pb1 – Br1	73.375(8)
Pb1 – Br1	3.2119(3)	Br1 – Pb1 – Br1	136.476(10)
Pb1 – Br1	3.2336(3)		

Table S5. A comparison of bond distances and angles in the $[PbBr_6]^{4-}$ octahedra in $[Cu(O_2C-(CH_2)_3-NH_3)_2]PbBr_4$.

Atom pair	Distance (Å)	Label	Angle (°)
Pb1 – Br3	2.8711(4)	Br3 – Pb1 – Br4	95.031(13)
Pb1 – Br4	2.9810(4)	Br3 – Pb1 – Br4	92.839(12)
Pb1 – Br4	2.9958(4)	Br4 – Pb1 – Br4	92.658(8)
Pb1 – Br2	3.0472(4)	Br3 – Pb1 – Br2	88.164(11)
Pb1 – Br2	3.0777(4)	Br4 – Pb1 – Br2	83.300(12)
Pb1 – Br1	3.0992(4)	Br4 – Pb1 – Br2	175.908(11)
		Br3 – Pb1 – Br2	86.988(11)
		Br4 – Pb1 – Br2	170.308(11)
		Br4 – Pb1 – Br2	96.714(13)
		Br2 – Pb1 – Br2	87.297(8)
		Br3 – Pb1 – Br1	168.661(12)
		Br4 – Pb1 – Br1	96.107(11)
		Br4 – Pb1 – Br1	88.764(11)
		Br2 – Pb1 – Br1	91.027(10)
		Br2 – Pb1 – Br1	81.676(10)

1. The fabricated X-ray detector and the setup used for the electrical measurements

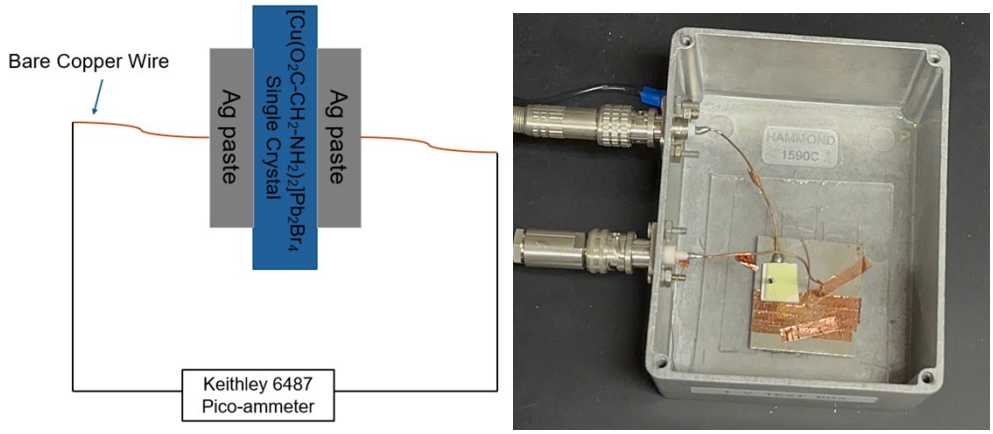

Figure S1. A schematic illustrating the fabricated X-ray detector in this work (left) and the setup used for electrical measurements (right).

The X-ray detector fabricated in this study is a planar-type detector with high-quality silver paste (purchased from Ted Pella, Inc.) manually brushed on the two opposite sides of a single crystal. Bare copper wires were attached to the crystal and then the crystal was connected to the Keithley 6487 pico-ammeter (an in-house built equipment, see Fig. S1 above) for conductivity and detector sensitivity measurements.

2. Images of $[Cu(O_2C\text{-}CH_2\text{-}NH_2)_2]Pb_2Br_4$ crystals grown using different methods

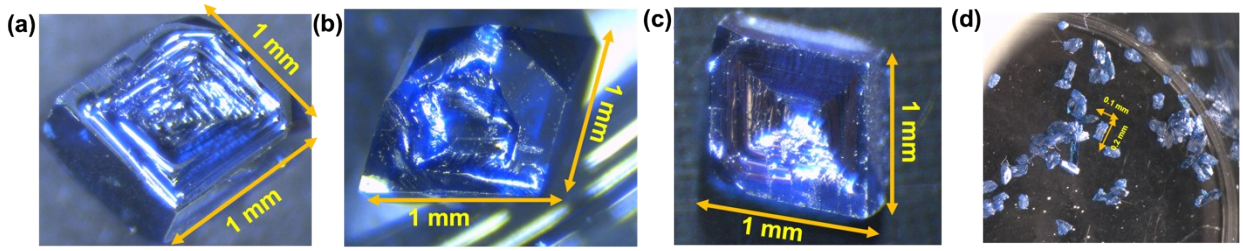

Figure S2. Photographs of the $[Cu(O_2C\text{-}CH_2\text{-}NH_2)_2]Pb_2Br_4$ crystals synthesized using (a) slow evaporation of solvent, (b) slow cooling of saturated solution, (c) evaporation of solvent on heating and (d) vapor diffusion.

3. Images of $[Cu(O_2C\text{-}CH_2\text{-}NH_2)_2]Pb_2Br_4$ crystals grown using the liquid-liquid diffusion method

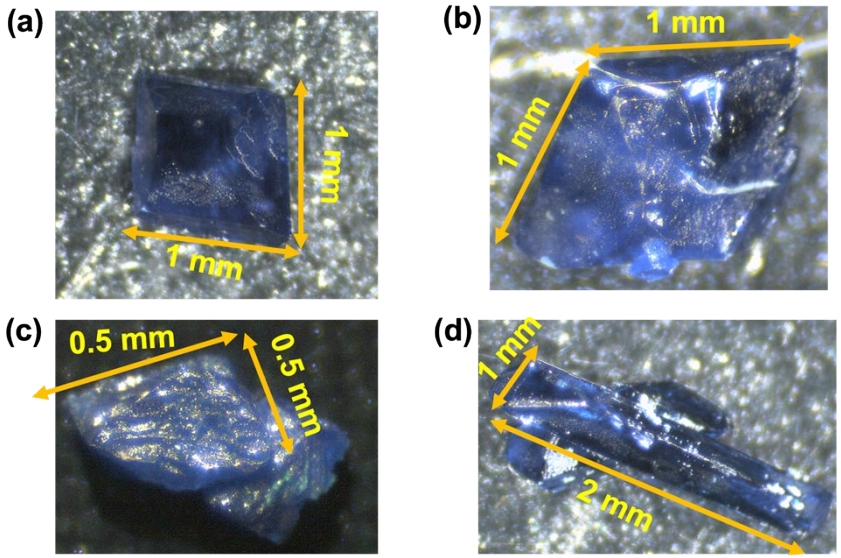

Figure S3. Photographs of the $[Cu(O_2C\text{-}CH_2\text{-}NH_2)_2]Pb_2Br_4$ crystals synthesized using liquid-liquid diffusion with solvents (a) isopropanol, (b) acetonitrile, (c) diethyl ether and (d) methanol.

4. Images of $[Cu(O_2C\text{-}(CH_2)_3\text{-}NH_3)_2]PbBr_4$ crystals obtained via different methods

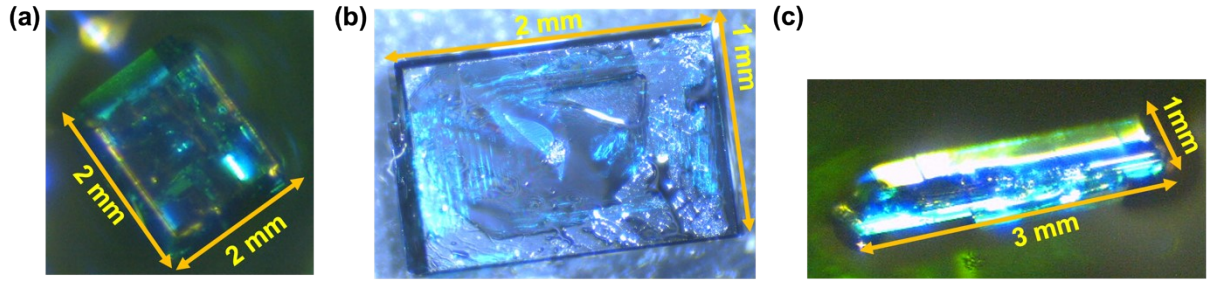

Figure S4. Photographs of the $[Cu(O_2C\text{-}(CH_2)_3\text{-}NH_3)_2]PbBr_4$ crystals synthesized using (a) slow evaporation of solvent, (b) slow cooling of saturated solution and (c) evaporation of solvent on heating.

5. Comparative analysis of PXRD patterns for crystals obtained via varied methods

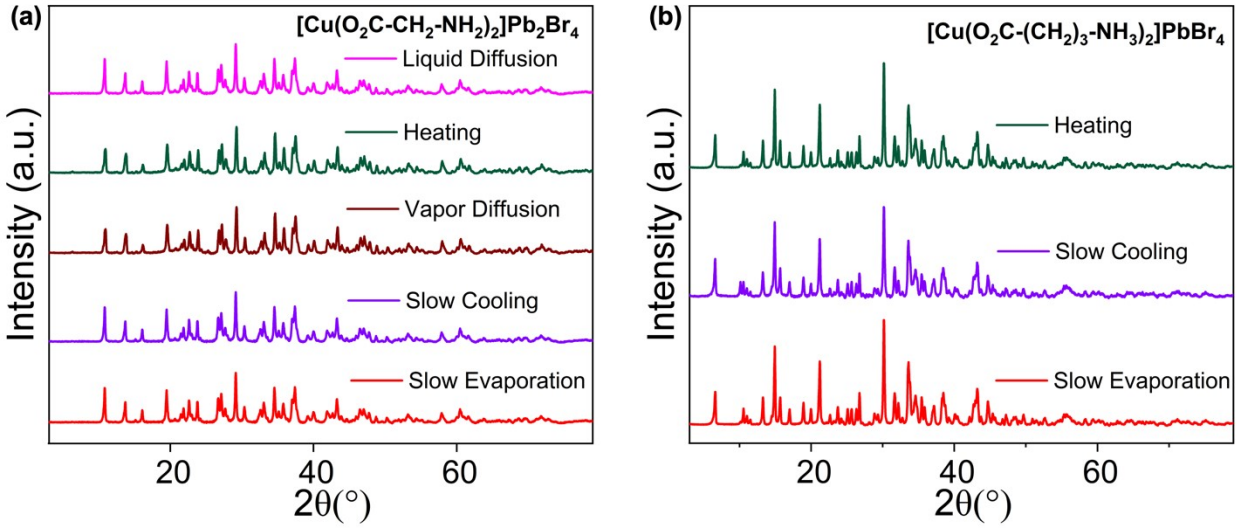

Figure S5. PXRD patterns showing the similarity between the synthesized crystals by using different solution synthesis methods for (a) $[Cu(O_2C\text{-}CH_2\text{-}NH_2)_2]Pb_2Br_4$ and (b) $[Cu(O_2C\text{-}(CH_2)_3\text{-}NH_3)_2]PbBr_4$ crystals.

6. Pawley fitting of Room Temperature PXRD patterns

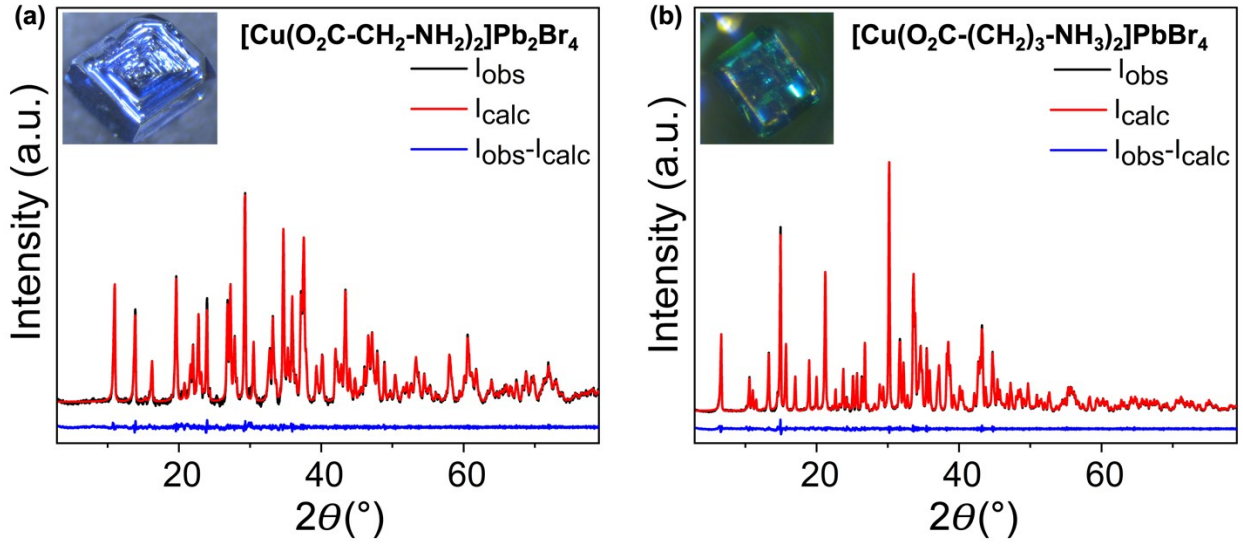

Figure S6. Room temperature PXRD patterns (in black) fitted using the Pawley method (in red) for (a) $[Cu(O_2C\text{-}CH_2\text{-}NH_2)_2]Pb_2Br_4$ and (b) $[Cu(O_2C\text{-}(CH_2)_3\text{-}NH_3)_2]PbBr_4$. Difference between the measured and calculated patterns are shown in blue.

7. Visualization of interlayer distances in $[Cu(O_2C\text{-}CH_2\text{-}NH_2)_2]Pb_2Br_4$ and $[Cu(O_2C\text{-}(CH_2)_3\text{-}NH_3)_2]PbBr_4$

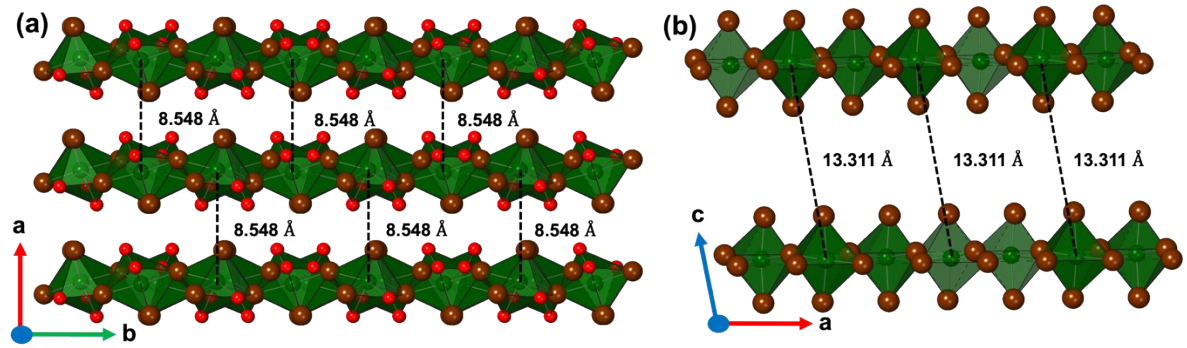

Figure S7. Interlayer distance between the layers of lead bromide in compounds (a) $[Cu(O_2C\text{-}CH_2\text{-}NH_2)_2]Pb_2Br_4$ and (b) $[Cu(O_2C\text{-}(CH_2)_3\text{-}NH_3)_2]PbBr_4$ are depicted. Lead, bromine, and oxygen are denoted by green, brown, and red spheres, respectively.

8. Visualization of interlayer distances in $(C_6H_5C_2H_4NH_3)_2PbBr_4$

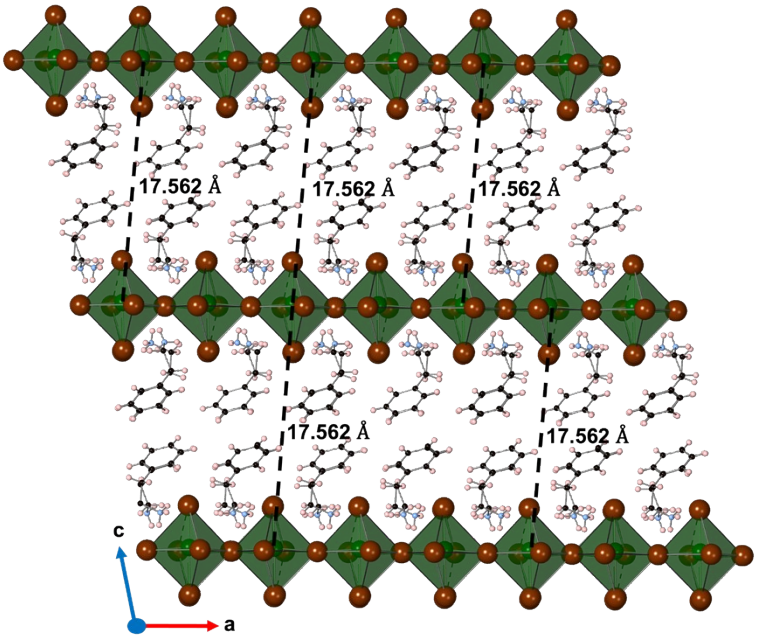

Figure S8. Interlayer distance between the layers of lead bromide in compound $(C_6H_5C_2H_4NH_3)_2PbBr_4$ is depicted within the crystal structure. Lead, bromine, oxygen, carbon, and hydrogen are denoted by green, brown, red spheres, black and peach, respectively.

9. UV-Vis absorption spectra for $[Cu(O_2C\text{-}CH_2\text{-}NH_2)_2]Pb_2Br_4$ and $[Cu(O_2C\text{-}(CH_2)_3\text{-}NH_3)_2]PbBr_4$ precursor solutions

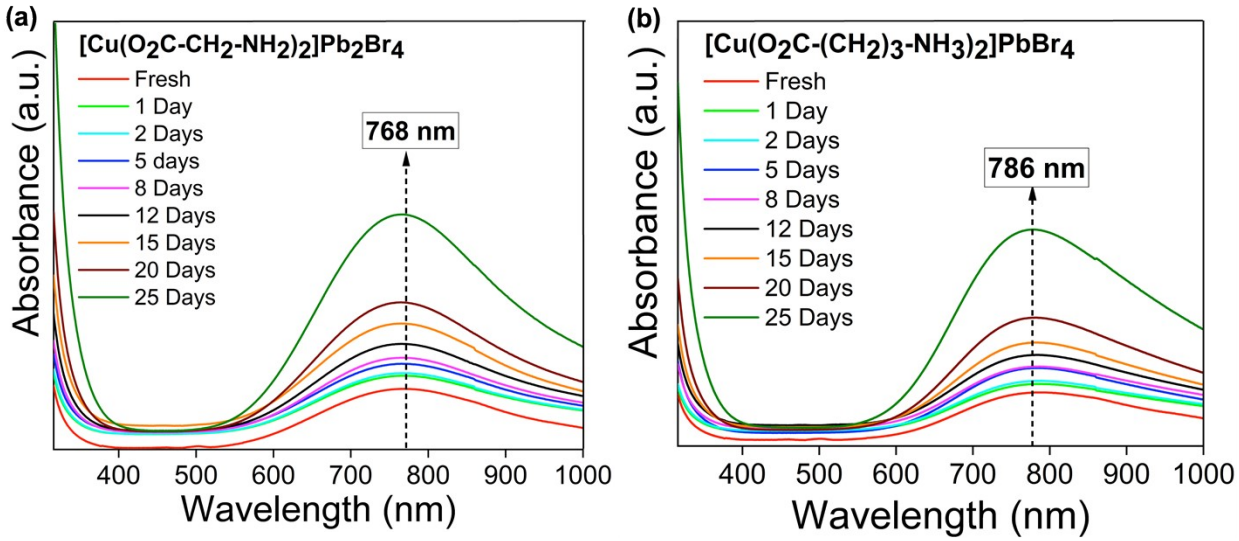

Figure S9. UV-Vis absorption spectra for $[Cu(O_2C\text{-}CH_2\text{-}NH_2)_2]Pb_2Br_4$ and (b) $[Cu(O_2C\text{-}(CH_2)_3\text{-}NH_3)_2]PbBr_4$ solutions in water.

A comparison of the absorption spectra suggests a red-shifted *d-d* absorption band with a peak maximum at 786 nm for $[Cu(O_2C\text{-}(CH_2)_3\text{-}NH_3)_2]PbBr_4$ compared to a peak maximum of 768 nm for $[Cu(O_2C\text{-}CH_2\text{-}NH_2)_2]Pb_2Br_4$.

10. Small-Angle X-Ray Scattering (SAXS)

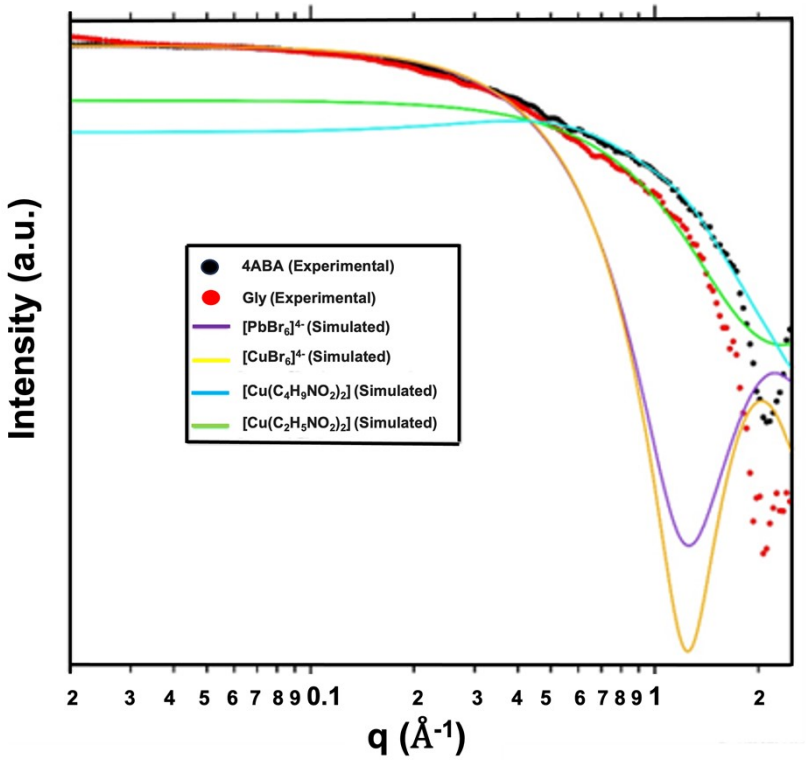

Figure S10. Measured SAXS data (red and black dotted lines) of $[Cu(O_2C\text{-}CH_2\text{-}NH_2)_2]Pb_2Br_4$ (labelled as Gly) and (b) $[Cu(O_2C\text{-}(CH_2)_3NH_3)_2]PbBr_4$ (labelled as 4ABA) compared to the simulated SAXS curves (solid lines) for $[PbBr_6]^{4-}$, $[CuBr_6]^{4-}$, $[Cu(C_4H_9NO_2)_2]$ and $[Cu(C_2H_5NO_2)_2]$.

The acquired SAXS curves for $[Cu(O_2C\text{-}CH_2\text{-}NH_2)_2]Pb_2Br_4$ and $[Cu(O_2C\text{-}(CH_2)_3\text{-}NH_3)_2]PbBr_4$ solutions agree well with the simulated curves of $[PbBr_6]^{4-}$ and $[CuBr_6]^{4-}$ in the range of q = 0.018−0.14 $Å^{-1}$ (Figure S9). Even though $CuBr_2$ was used in a ~10-fold excess compared to $PbBr_2$ in each solution, the high electron density of Pb implied that both species could contribute substantial scattering in this region. Above q = 0.14 $Å^{-1}$, scattering from less electron dense species was observed and attributed to Cu/amino acid complexes. The experimental curve of $[Cu(O_2C\text{-}(CH_2)_3\text{-}NH_3)_2]PbBr_4$ overlapped with the simulated curve of $[Cu(C_4H_9NO_2)_2]$ from q = 0.15−1.7 $Å^{-1}$, and the experimental curve of $[Cu(O_2C\text{-}CH_2\text{-}NH_2)_2]Pb_2Br_4$ overlapped with the simulated curve of $[Cu(C_2H_5NO_2)_2]$ from q = 0.15−1.3 $Å^{-1}$. Based on the agreement with simulated scattering curves in the low and high q regions, SAXS of $[Cu(O_2C\text{-}CH_2\text{-}NH_2)_2]Pb_2Br_4$ and $[Cu(O_2C\text{-}(CH_2)_3\text{-}NH_3)_2]PbBr_4$ suggested a mixture of small solution species was present in both samples before crystallization. This was further confirmed by ESI-MS studies.

11. ESI-MS measurement results

The ESI-MS of $[Cu(O_2C\text{-}CH_2\text{-}NH_2)_2]Pb_2Br_4$ in positive mode produced more extensive fragmentation than $[Cu(O_2C\text{-}(CH_2)_3\text{-}NH_3)_2]PbBr_4$ which impeded the detection of any Cu/glycine/Br species. The fragmentation of glycine in mass spectrometry is well noted and various pathways have studied.[1] For $[Cu(O_2C\text{-}(CH_2)_3\text{-}NH_3)_2]PbBr_4$, several Cu/4-aminobutyric acid/Br species were identified in the positive mode of ESI-MS (Table S7) and various Cu/Br species were identified in the negative mode of both $[Cu(O_2C\text{-}(CH_2)_3\text{-}NH_3)_2]PbBr_4$ and $[Cu(O_2C\text{-}CH_2\text{-}NH_2)_2]Pb_2Br_4$ (Table S6 and S8). Interestingly, one Pb/Br species, i.e., $[PbBr_3]^-$, was also observed in the negative mode of ESI-MS of both $[Cu(O_2C\text{-}CH_2\text{-}NH_2)_2]Pb_2Br_4$ and $[Cu(O_2C\text{-}(CH_2)_3\text{-}NH_3)_2]PbBr_4$ with small relative abundances of 0.11% and 0.50% respectively, which could have been due to small relative concentration or ionization potential. Cu species were observed with Cu(I) and Cu(II) reflecting the redox behavior occasionally seen in ESI-MS. In agreement with SAXS, ESI-MS of $[Cu(O_2C\text{-}CH_2\text{-}NH_2)_2]Pb_2Br_4$ and $[Cu(O_2C\text{-}(CH_2)_3\text{-}NH_3)_2]PbBr_4$ suggested a mixture of small solution species was present in both samples. Furthermore, these results showed that Cu/Pb/Br species were more likely to form negative charges while Cu/amino acid/Br species were more likely to form positively charges.

Table S6. The results of ESI-MS studies for negative mode of $[Cu(O_2C\text{-}(CH_2)_3NH_3)_2]PbBr_4$ solution.

Experimental m/z	R.A. (%)	Identified species	Calc. m/z
80.9226	26.4	$[Br]^-$	80.9168
160.8525	0.73	$[HBr_2]^-$	160.843
222.7780	100	$[CuBr_2]^-$	222.7648
303.6991	8.49	$[CuBr_3]^-$	303.6811
366.6322	66.71	$[Cu_2Br_3]^-$	366.6108
446.7573	0.11	$[PbBr_3]^-$	446.7288
447.5534	4.04	$[Cu_2Br_4]^-$	447.5271
510.4859	11.94	$[Cu_3Br_4]^-$	510.4568
589.4093	2.69	$[Cu_3Br_5]^-$	589.3751
654.3395	3.41	$[Cu_4Br_5]^-$	654.3028
796.1949	3.55	$[Cu_5Br_6]^-$	796.1507
940.0491	1.91	$[Cu_6Br_7]^-$	939.9967
1083.9023	0.70	$[Cu_7Br_8]^-$	1083.8427

Table S7. The results of ESI-MS studies for positive mode of $[Cu(O_2C\text{-}(CH_2)_3NH_3)_2]PbBr_4$ solution.

Experimental m/z	R.A. (%)	Identified species	Calc. m/z
62.908	8.7	$[Cu]^+$	62.9291
86.0377	54.61	$[HO_2C_4H_5]^+$	86.0362
87.022	54.72	$[HO_2C_4H_6]^+$	87.0441
104.0478	86.7	$[HO_2C_4H_6NH_3]^+$	104.0706
165.9705	76.54	$[Cu(O_2C_4H_6NH_3)]^+$	165.9924
246.8913	3.34	$[CuBr(O_2C_4H_6NH_3)]^+$	246.9088
268.0315	2.08	$[Cu(O_2C_4H_6NH_2)_2H]^+$	268.0479
274.2589	100	$[C_{16}H_{36}NO_2]^{+[a]}$	274.2741
318.2878	11.08	$[C_{18}H_{40}NO_3]^{+[a]}$	318.3003
329.9588	16.15	$[Cu_2(O_2C_4H_6NH_2)_2]^+$	329.9697
330.9639	9.36	$[Cu_2(O_2C_4H_6NH_2)_2H]^+$	330.9775
410.8826	10.37	$[Cu_2Br(O_2C_4H_6NH_2)_2]^+$	410.8861
411.8891	3.95	$[Cu_2Br(O_2C_4H_6NH_2)_2H]^+$	411.8939
473.8176	9.31	$[Cu_3Br(O_2C_4H_6NH_2)_2]^+$	473.8157

[a] $[C_{16}H_{36}NO_2]^+$ and $[C_{18}H_{40}NO_3]^+$ have previously been identified as contaminants leached from plastic centrifuge tubes[2] which likely occurred due to HBr incompatibility.

Table S8. The results of ESI-MS studies for negative mode of $[Cu(O_2C\text{-}CH_2\text{-}NH_2)_2]Pb_2Br_4$ solution.

Experimental m/z	R.A. (%)	Identified species	Calc. m/z
80.9226	37.88	$[Br]^-$	80.9168
160.8530	1.19	$[HBr_2]^-$	160.8430
222.7780	100	$[CuBr_2]^-$	222.7648
303.6991	11.86	$[CuBr_3]^-$	303.6811
366.6324	59.32	$[Cu_2Br_3]^-$	366.6108
446.7542	0.50	$[PbBr_3]^-$	446.7288
447.5530	4.85	$[Cu_2Br_4]^-$	447.5271
510.4860	15.19	$[Cu_3Br_4]^-$	510.4568
589.4082	5.60	$[Cu_3Br_5]^-$	589.3751
654.3394	5.22	$[Cu_4Br_5]^-$	654.3028
796.1953	4.15	$[Cu_5Br_6]^-$	796.1507
940.0494	1.92	$[Cu_6Br_7]^-$	939.9967
1083.9050	0.89	$[Cu_7Br_8]^-$	1083.8427

12. PXRD data for $(C_6H_5C_2H_4NH_3)_2PbBr_4$

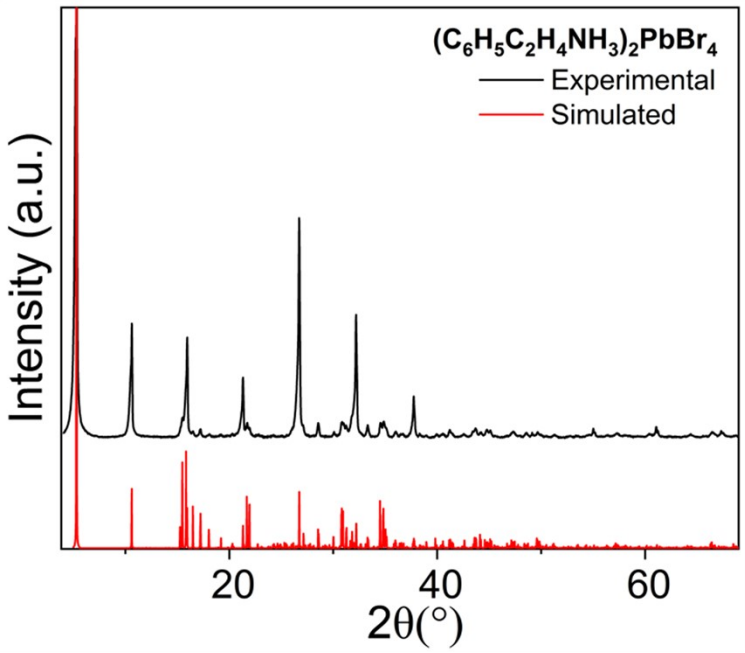

Figure S11. PXRD patterns of single crystals synthesized via slow cooling method, compared to the calculated (simulated) XRD pattern for $(C_6H_5C_2H_4NH_3)_2PbBr_4$.

13. Air stability assessment through PXRD patterns of synthesized crystals

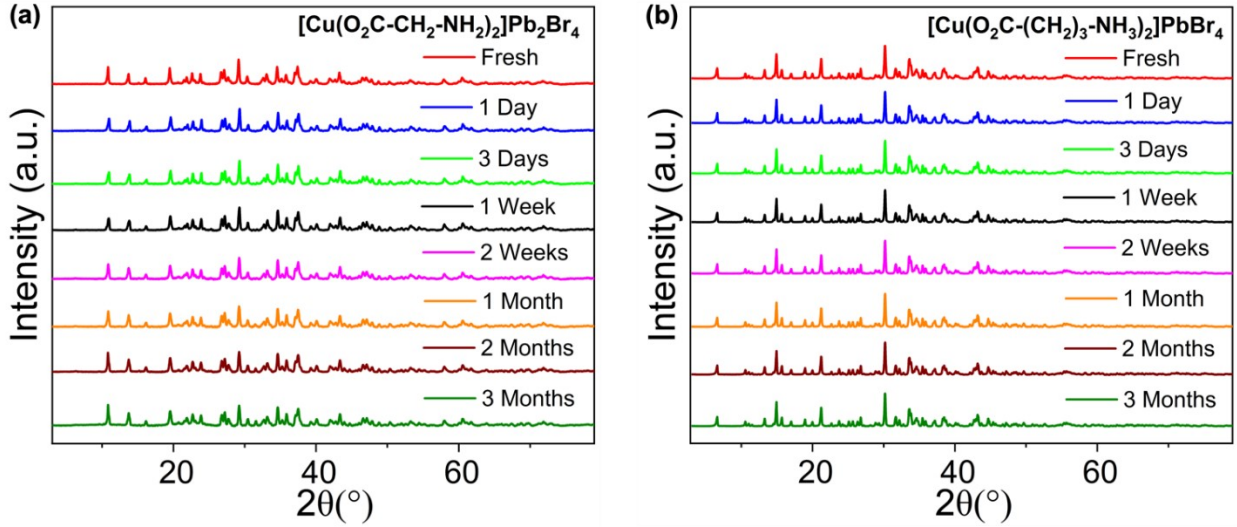

Figure S12. PXRD patterns of synthesized (a) $[Cu(O_2C\text{-}CH_2\text{-}NH_2)_2]Pb_2Br_4$ and (b) $[Cu(O_2C\text{-}(CH_2)_3\text{-}NH_3)_2]PbBr_4$ crystals using slow evaporation method for 3 months.

14. Air stability assessment through PXRD patterns of $(C_6H_5C_2H_4NH_3)_2PbBr_4$ crystals

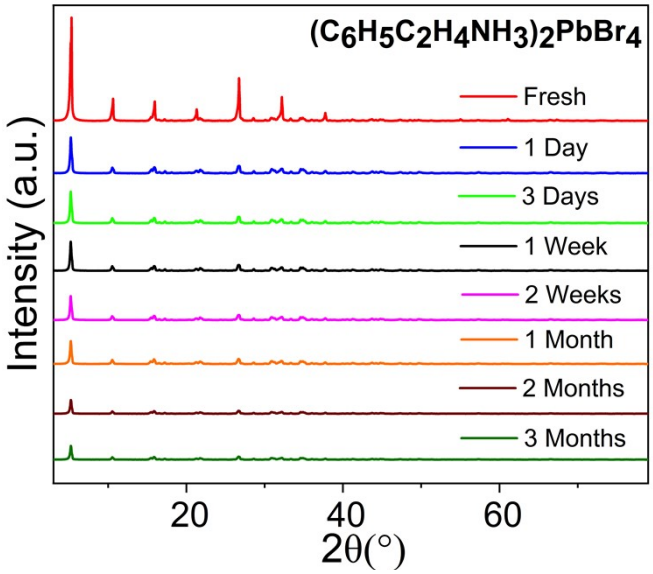

Figure S13. PXRD patterns of synthesized $(C_6H_5C_2H_4NH_3)_2PbBr_4$ crystals using slow cooling method for 3 months.

15. Diffuse reflectance and TGA/DSC data for $(C_6H_5C_2H_4NH_3)_2PbBr_4$

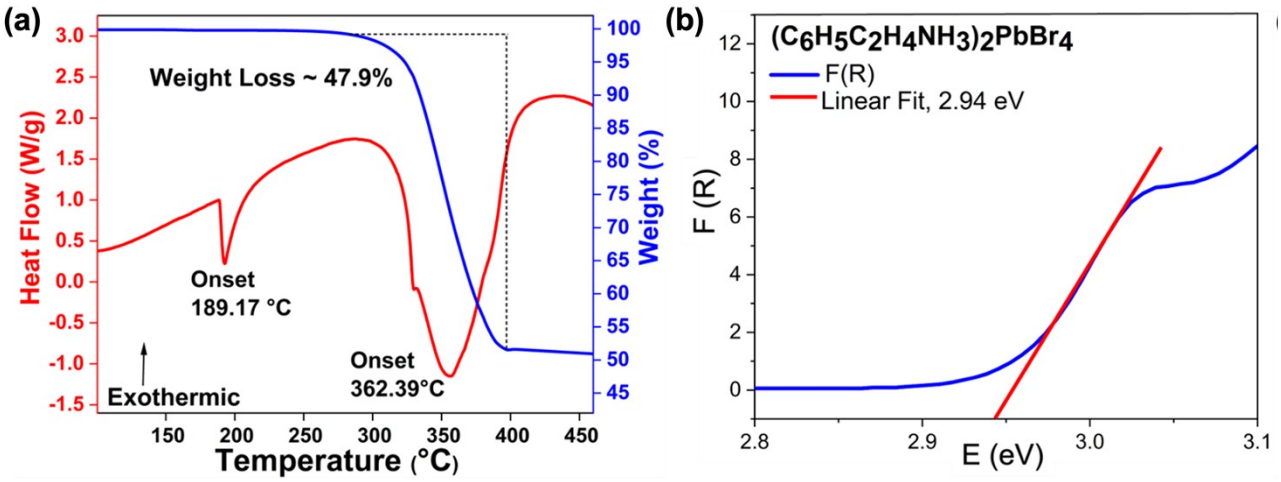

Figure S14. (a) Thermogravimetric analysis (TGA) and Differential Scanning Calorimetry (DSC) curves are presented in blue and red, respectively, for $(C_6H_5C_2H_4NH_3)_2PbBr_4$ and (b) Optical absorption information was acquired using the Kubelka-Munk function, denoted as F(R).

References

(1) O'Hair, R. A.; Broughton, P. S.; Styles, M. L.; Frink, B. T.; Hadad, C. M. The fragmentation pathways of protonated glycine: a computational study. *J Am Soc for Mass Spectrom* **2000**, *11* (8), 687-696.
(2) Chai, Y.; Chen, H.; Gao, G.; Liu, X.; Lu, C. Identification of new interferences leached from plastic microcentrifuge tubes in electrospray ionization mass spectrometry. *Rapid Commun. Mass Spectrom.* **2019**, *33* (10), 969-977.